Orbit Determination for Low-Altitude Satellites Using Semianalytical Satellite Theory

Rodrigo Moreira de Oliveira
rodrigo.d.oliveira@tecnico.ulisboa.pt

Instituto Superior Técnico, Universidade de Lisboa, Portugal

January 2021

Abstract

The tracking of spacecraft provided by Orbit Determination systems requires frequent and accurate monitoring of their orbital trajectories, which, in many cases, is fundamental to the success and deliverance of space missions. This thesis focuses on the problem of sequential real-time estimation of a Low Earth Orbit satellite (with applications in remote sensing, communications, Earth observation, etc.) tracked by ground stations. Although the use of GNSS sensors has been favored in recent years for this kind of mission scenario due to their low-cost, availability and proven capability of satellite tracking, these systems might not always be reliable. In view of this, it is necessary to provide auxiliary systems that safeguard Orbit Determination procedures in case of GNSS failure. This thesis combines the Semianalytical Satellite Theory with current Kalman filtering techniques to develop and study two sequential algorithms: the Extended Semianalytical Kalman Filter and the Unscented Semianalytical Kalman Filter. The latter is a novel algorithm proposed in this research, combining semianalytical propagation with Unscented Kalman Filters. The design implications of the interaction between these filters and the orbital propagation/perturbation theory are discussed. These algorithms are then evaluated in terms of efficiency, accuracy and speed of convergence by comparison with Special Perturbation Cowell Extended and Unscented Kalman Filters, which are more established algorithms in the literature. By conducting some simulation test cases, it is found that Semianalytical filters can compete with Cowell filters in accurately and efficiently determining and predicting satellite ephemerides.
Keywords: Orbit Determination, Kalman Filters, Low Earth Orbit, Semianalytical Propagation, Cowell Propagation

1. Introduction

Satellite Orbit Determination (OD) refers to the estimation of orbits of space objects, given applicable measurements [1]. OD has had a long and outstanding history. From the launch in 1957 of Sputnik, which was tracked mostly by visual observations with a precision to only a few kilometers, the technological revolution of the last decades (in terms of computational power and tracking sensors) has enable OD solutions to the reach sub-centimeter accuracy [1].

A broad number of satellite space missions and applications require orbit information provided by OD systems (Earth observation, remote sensing, telecommunications, etc.) [2]. OD estimates are also crucial for orbit control and planning [3].

In recent years there has been a large increase in the populations of satellites around the Earth. This growth demands the development and improvement of fast, efficient and accurate orbit propagators. It is estimated that the US Joint Space Operation Center performs about 40 000 track and object correlations per day to maintain their catalog and provide collision warnings [4]. Broadly speaking, orbit propagation methods are classified as [5]: 1) Special Perturbation (SP) methods numerically and accurately propagate the Equations of Motion (EoM); 2) General Perturbation (GP) methods provide analytical and simplified approximations to the EoM; and 3) Semianalytical methods average the EoM, explicitly separating the short-term periodic motion from the long-term periodic and secular motion, which can then be numerically propagated with much larger integration step sizes when compared to SP. SP methods are the most accurate, but also the most computationally demanding, whereas GP methods are efficient but much more inaccurate [4]. Semianalytical methods provide a middle ground of sorts between SP and GP.

This work focuses on the problem of sequential real-time OD of a Low Earth Orbit (LEO) satellite tracked by ground stations implementing both

SP and Semianalytical propagation schemes. Although the use of GNSS has been greatly favored in past years, it is important to provide auxiliary systems that safeguard OD procedures in case of GNSS failure. Reduced force models are considered, and these dynamics are then coupled with established nonlinear and sub-optimal filtering schemes, namely, the Extended Kalman Filter (EKF) and the Unscented Kalman Filter (UKF).

While SP and GP propagation schemes have been extensively studied in the context of OD [5, 6, 7, 8], only a handful of research studies have been concerned with coupling OD filters with Semianalytic Satellite Theory (SST) [9, 10, 11]. Andrew Green in [9] and Stephen Taylor in [10] proposed, implemented and tested the coupling of an EKF filter with Draper Semianalytical Satellite Theory (DSST) [12]. Besides reproducing this Extended Semianalytical Kalman Filter (ESKF), this work proposes a novel algorithm coupling an UKF with SST. The performance of these Semianalytical filters is evaluated and benchmarked against traditional implementations of Cowell filters (EKF and UKF). The SST used in this research is based on recent work by Todd Ely [13, 14]. When compared to DSST, Ely's theory is more flexible, easier to implement in computational applications and covers a wider range of problem domains, namely, eccentric orbits [13].

The development of Semianalytical OD systems require additional operations (when compared to SP methods) to keep their efficient implementation.

2. Propagation and Measurement Models

In order to build orbital propagation and measurement models, a state-space representation of the satellite dynamics is needed. The two state-space models required for this work are summarized below.

2.1. Orbital State-Space Models

Six unidimensional quantities are needed to define the state of spacecraft (without orientation), building up different orbital state-space models. These models are either built around generic position and velocity vectors, or orbital element sets, which are scalar magnitude and angular variables that specify the shape and orientation of the orbit and locate the satellite within it.

Let $\mathbf{x}$ denote the orbital state vector, comprising the Earth Centered Inertial (ECI) position $\boldsymbol{r}_i$ and velocity $\boldsymbol{v}_i$, expressed in Cartesian coordinates, i.e.,

$$\mathbf{x} = \left[x, y, z, v_x, v_y, v_z\right]^T .$$

SST is usually developed in the equinoctial element set, which is denoted as $\boldsymbol{\mathcal{E}} = [a, h, k, p, q, \lambda]^T$. Either representation is equivalent and completely locates the object.

2.2. Osculating Dynamics

This work adopts a reduced force model that is suitable for real-time implementation and captures the most important perturbations from the Earth's gravitational field and atmospheric drag. Resorting to *Cowell's formulation* [5], the inertial osculating satellite acceleration is given by

$$\ddot{\boldsymbol{r}}_i(t) = \boldsymbol{a}_i(t) = \boldsymbol{a}_{i\ \text{Earth grav.}}(t) + \boldsymbol{a}_{i\ \text{drag}}(t) . \quad (1)$$

The continuous-time osculating orbital propagation model, using the state vector $\mathbf{x}$, is then

$$\dot{\mathbf{x}}(t) = \begin{bmatrix} \boldsymbol{v}_i(t) \\ \boldsymbol{a}_i(t) \end{bmatrix} = \boldsymbol{f}(\mathbf{x}(t), t) + \boldsymbol{w}(t) , \quad (2)$$

where $\boldsymbol{w}$ is the process noise sequence that accounts for the uncertainty error in truncating the force model. It is assumed to be a white, zero-mean Gaussian noise process, with covariance (power spectral density) $\boldsymbol{Q}_{\mathbf{x}}(t)$.

The acceleration vectors $\boldsymbol{a}_{i\ \text{Earth grav.}}$ and $\boldsymbol{a}_{i\ \text{drag}}$ are modeled next.

2.2.1 Earth's Gravitational Field

The gravitational potential can be expressed in functional form as $U = U(\boldsymbol{r}_f, \nu)$, where ν is a vector of model parameters and $\boldsymbol{r}_f$ is the satellite position in the Earth Centered Earth Fixed (ECEF) frame. The spatial gradient of U with respect to $\boldsymbol{r}_f$ yields [6]

$$\boldsymbol{a}_{f\ \text{Earth grav.}} = \left[\frac{\partial U(\boldsymbol{r}_f, \nu)}{\partial \boldsymbol{r}_f}\right]^T . \quad (3)$$

The expression above is the inertial acceleration in an inertial frame aligned with ECEF, and thus, a rotation is needed to obtain the acceleration aligned with ECI coordinates, i.e., $\boldsymbol{a}_{i\ \text{Earth grav.}} = \boldsymbol{T}_f^i \boldsymbol{a}_{f\ \text{Earth grav.}}$, where $\boldsymbol{T}_f^i$ is the rotation matrix from ECEF to ECI.

Taking into account the Earth's non-uniform mass distribution and non-spherical shape and symmetry, U is expressed as a function of the orbiter's ECEF geocentric coordinates $[r, \phi_{gc}, \lambda]^T$ modeled with the following spherical harmonic series [5]

$$\begin{aligned} U = &\frac{\mu_\oplus}{r}\Bigg[1 + \sum_{n=2}^{N_n} C_{n,0} \left(\frac{a_e}{r}\right)^n P_{n,0}\left(\sin\phi_{gc}\right) \\ &+ \sum_{n=2}^{N_n} \sum_{m=1}^{\min(n,N_m)} \left(\frac{a_e}{r}\right)^n P_{n,m}\left(\sin\phi_{gc}\right)\left[C_{n,m}\cos(m\lambda)\right. \\ &\left. + S_{n,m}\sin(\lambda)\right]\Bigg] , \end{aligned} \quad (4)$$

Each harmonic (term in the series) is specified by its degree and order (n, m), classified as zonal if $m = 0$, as sectoral if $n = m$, or as tesseral if $n \neq m \neq 0$. In computational applications, the series is truncated at a certain finite degree N_n and order N_m. a_e is a reference radius, usually taken as the mean equatorial radius $R_\oplus$. $C_{n,m}$ and $S_{n,m}$ are the gravitational coefficients, and $P_{n,m}(u)$ are the Associated Legendre Functions (ALFs). In this work, the gravitational coefficients are provided by the EGM-96 gravitational model.

2.2.2 Atmospheric Drag

Atmospheric drag is also a strong influence on the motion of LEO satellites [6]. The general equation for aerodynamic drag is

$$\boldsymbol{a}_{i\ \mathrm{drag}} = -\frac{1}{2}\frac{C_D A}{m}\rho \left\|\boldsymbol{v}_{\mathrm{rel.}}\right\| \boldsymbol{v}_{\mathrm{rel.}}\,, \tag{5}$$

where C_D is the coefficient of drag, A is the satellite's cross-sectional area, m is its mass and ρ is the atmospheric density. $\boldsymbol{v}_{\mathrm{rel.}}$ is the velocity of the satellite relative to the local surrounding atmosphere. A reasonable approximation is to assume that the atmosphere co-rotates with the Earth [6], resulting in $\boldsymbol{v}_{\mathrm{rel.}} = \boldsymbol{v}_i - \boldsymbol{\omega}_\oplus \times \boldsymbol{r}_i$, where $\boldsymbol{\omega}_\oplus$ is the Earth's angular velocity vector. In this work, the atmosphere is modeled with the *Exponential Model*, cf. [5].

2.3. Mean Dynamics

The underlying idea of Semianalytical propagation is to separate short-term from long-term periodic and secular motion, obtaining the mean dynamics, which can, in turn, be numerically propagated with much larger step sizes. The decoupling of short-periodic motion from the EoM is based on the Generalized Method of Averaging of nonlinear dynamical systems [15].

Mean dynamics are commonly modeled with the equinoctial set $\boldsymbol{\mathscr{E}}$. Let $\boldsymbol{\mathscr{E}} = [\boldsymbol{\alpha}^T, \lambda]$, where vector $\boldsymbol{\alpha} = [a, h, k, p, q]$ denotes the slowly-varying equinoctial elements, that indicate the orbit's shape and orientation, and λ denotes the fast variable, that locates the satellite in the orbit. Furthermore, the osculating elements, $\boldsymbol{\mathscr{E}}$, are distinguished from the mean elements, $\bar{\boldsymbol{\mathscr{E}}}$, with an overbar.

The osculating equinoctial EoM are obtained by converting (1) to equinoctial form. The Gaussian Variation-of-Parameters (VOP) formulation is given by [12]

$$\dot{\mathscr{E}}_i = \frac{\mathrm{d}\mathscr{E}_i}{\mathrm{d}t} = n(a)\delta_{i6} + \frac{\mathrm{d}\mathscr{E}_i}{\mathrm{d}\boldsymbol{v}} \sum_{p\in P} \boldsymbol{q}_p\,, \quad i = 1,\ldots,6\,, \tag{6}$$

where $\sum_{p\in P} \boldsymbol{q}_p$ is the vector sum of all perturbing inertial accelerations $\boldsymbol{q}_p$, $\boldsymbol{v}$ is the inertial osculating satellite velocity and δ_{ij} denotes the Kronecker delta. The perturbations to be considered are, as in Section 2.2, due to the Earth's gravitational field and drag, therefore the set of active perturbations is $P = \{Z, T, D\}$, where Z denotes the zonal harmonics, T the tesseral/sectoral harmonics and D drag. Partials $\partial\boldsymbol{\mathscr{E}}/\partial\boldsymbol{v}$ may be found in [12]. $n(a) = \sqrt{\mu_\oplus/a^3}$ is the osculating mean motion.

Averaging tesseral/sectoral perturbing acceleration requires special treatment, since these perturbations are also dependent on the central body's orientation relative to the spacecraft. This dependence is usually expressed via the sidereal angle θ. In Earth's case, this is generally a fast dependence. The present work resorts to the study of non-resonant tesseral and sectoral harmonics. Inclusion of resonances is left as future work.

The mean EoM are found by averaging (6) with respect to the fast variable λ (and θ for tesseral/sectoral perturbations). This process is briefly summarized below.

2.3.1 Averaging the Equations of Motion

The mean EoM are built on the assumption that the mean dynamics take the following VOP form

$$\frac{\mathrm{d}\bar{\mathscr{E}}_i}{\mathrm{d}t} = n(\bar{a})\delta_{i6} + \sum_{j=1}^{\infty} \epsilon^j A_i^j(\bar{\boldsymbol{\alpha}})\,, \quad i = 1,\ldots,6\,. \tag{7}$$

Functions $\epsilon^j A_i^j$ are the slowly-varying mean element rates of change[1] due to the perturbing forces, and are not dependent on the fast variables. ϵ is a small variational parameter. Truncating (7) to first order in ϵ, the averaged rates A_i^1 are given by [12]

$$\begin{aligned} A^1_{i_{Z,D}}(\bar{\boldsymbol{\alpha}}) &= \frac{1}{2\pi}\int_{\bar{\lambda}}^{\bar{\lambda}+2\pi} F_{i_{Z,D}}(\bar{\boldsymbol{\alpha}},\xi)d\xi\,.\,, \\ A^1_{i_T}(\bar{\boldsymbol{\alpha}}) &= \frac{1}{4\pi^2}\int_{\theta}^{\theta+2\pi}\int_{\bar{\lambda}}^{\bar{\lambda}+2\pi} F_{i_T}(\bar{\boldsymbol{\alpha}},\xi,\psi)d\xi\, d\psi\,, \end{aligned} \tag{8}$$

where:

$$\begin{aligned} F_{i_{Z,D}}(\bar{\boldsymbol{\alpha}},\bar{\lambda}) &= \frac{\mathrm{d}\mathscr{E}_i}{\mathrm{d}\boldsymbol{v}} \sum_{p\in\{Z,D\}} \boldsymbol{q}_p\,, \\ F_{i_T}(\bar{\boldsymbol{\alpha}},\bar{\lambda},\theta) &= \frac{\mathrm{d}\mathscr{E}_i}{\mathrm{d}\boldsymbol{v}}\boldsymbol{q}_T\,. \end{aligned} \tag{9}$$

It is noted that the osculating rate functions $F_{i_{Z,D}}(\bar{\boldsymbol{\alpha}},\bar{\lambda})$ are small and 2π-periodic in $\bar{\lambda}$, and the functions $F_{i_T}(\bar{\boldsymbol{\alpha}},\bar{\lambda},\theta)$ are small and 2π-periodic in both $\bar{\lambda}$ and θ. Furthermore, they are evaluated with the available mean state $\bar{\boldsymbol{\mathscr{E}}}$.

Following [13], the functions $A^1_{i_{Z,D}}$ are found with a classic Gaussian fixed-order numerical quadrature. Furthermore, it also shown in [13] that the non-resonant tesseral/sectoral harmonics average zero, i.e., $A^1_{i_T}(\bar{\boldsymbol{\alpha}}) = 0$.

[1] Notice that the superscript j in ϵ^j designates a power and in A_i^j designates an index.

2.3.2 Mean-to-Osculating Map

The osculating elements $\boldsymbol{\mathscr{E}}$ may be recovered with the mean-to-osculating map. Considering the set of active perturbations, this map is given by

$$\mathscr{E}_i = \bar{\mathscr{E}}_i + \sum_{j=1}^{\infty} \epsilon^j \left(\eta^j_{i_{Z,D}}(\bar{\boldsymbol{\alpha}}, \bar{\lambda}) + \eta^j_{i_T}(\bar{\boldsymbol{\alpha}}, \bar{\lambda}, \theta) \right), \quad i = 1, \ldots, 6 . \tag{10}$$

where η^j_i is the short-periodic variation of order j on element i. In the present work, this map is also truncated to first order.

As shown in [14], the zonal and drag contributions to the map are given by:

$$\begin{aligned} \eta^1_{i_{Z,D}}(\bar{\boldsymbol{\alpha}}, \bar{\lambda}) &= \frac{1}{n(\bar{a})} \sum_{\substack{k=-\infty \\ k \neq 0}}^{\infty} \frac{\mathcal{F}^k_{i_{Z,D}}(\bar{\boldsymbol{\alpha}})}{jk} e^{jk\bar{\lambda}} , \quad i = 1, \ldots, 5 , \\ \eta^1_{6_{Z,D}}(\bar{\boldsymbol{\alpha}}, \bar{\lambda}) &= \frac{1}{n(\bar{a})} \sum_{\substack{k=-\infty \\ k \neq 0}}^{\infty} \left[\frac{\mathcal{F}^k_{6_{Z,D}}(\bar{\boldsymbol{\alpha}})}{jk} + \frac{3}{2\bar{a}} \frac{\mathcal{F}^k_{1_{Z,D}}(\bar{\boldsymbol{\alpha}})}{k^2} \right] e^{jk\bar{\lambda}} , \end{aligned} \tag{11}$$

whereas the non-resonant tesseral/sectoral contributions are given by:

$$\begin{aligned} \eta^1_{i_T}(\bar{\boldsymbol{\alpha}}, \bar{\lambda}, \theta) &= \sum_{k=-\infty}^{\infty} \sum_{\substack{m=-N_m \\ m \neq 0}}^{N_m} \left[\frac{\mathcal{F}^{k,m}_{i_T}(\bar{\boldsymbol{\alpha}})}{j(kn(\bar{a}) - m\omega_\oplus)} \cdot e^{j(k\bar{\lambda} - m\theta)} \right], \quad i = 1, \ldots, 5 , \\ \eta^1_{6_T}(\bar{\boldsymbol{\alpha}}, \bar{\lambda}, \theta) &= \sum_{k=-\infty}^{\infty} \sum_{\substack{m=-N_m \\ m \neq 0}}^{N_m} \left[\frac{\mathcal{F}^{k,m}_{6_T}(\bar{\boldsymbol{\alpha}})}{j(kn(\bar{a}) - m\omega_\oplus)} + \frac{3n(\bar{a})}{2\bar{a}} \frac{\mathcal{F}^{k,m}_{1_T}(\bar{\boldsymbol{\alpha}})}{(kn(\bar{a}) - m\omega_\oplus)^2} \right] e^{j(k\bar{\lambda} - m\theta)} . \end{aligned} \tag{12}$$

To derive these expressions, it is necessary to expand the rates $F_{i_{Z,D}}(\bar{\boldsymbol{\alpha}}, \bar{\lambda})$ in 1-D Fourier Series (FS) as functions of $\bar{\lambda}$, and to expand the rates $F_{i_T}(\bar{\boldsymbol{\alpha}}, \bar{\lambda}, \theta)$ in 2-D FS as functions of $\bar{\lambda}$ and θ. Then, $\mathcal{F}^k_{i_{Z,D}}$ and $\mathcal{F}^{k,m}_{i_T}$ are, respectively, the associated FS coefficients.

According to [14], the coefficients $\mathcal{F}^k_{i_{Z,D}}$ and $\mathcal{F}^{k,m}_{i_T}$ are approximated by $X^k_{i_{Z,D}}$ and $X^{k,m}_{i_T}$, which are, respectively, the Discrete Fourier Transforms (DFTs) of $F_{i_{Z,D}}(\bar{\boldsymbol{\alpha}}, \bar{\lambda})$ and $F_{i_T}(\bar{\boldsymbol{\alpha}}, \bar{\lambda}, \theta)$.

The DFTs are performed efficiently using Fast Fourier Transform (FFT) algorithms.

2.3.3 Semianalytical Propagation Model

The continuous-time mean orbital propagation model is rewritten in a more compact form,

$$\dot{\bar{\boldsymbol{\mathscr{E}}}}(t) = \frac{\mathrm{d}\bar{\boldsymbol{\mathscr{E}}}}{\mathrm{d}t} = \bar{\boldsymbol{f}}(\bar{\boldsymbol{\mathscr{E}}}(t), t) + \bar{\boldsymbol{w}}(t) , \tag{13}$$

where $\bar{\boldsymbol{w}}(t)$ is the process noise sequence that accounts for the uncertainty error in the mean state propagation. It is assumed to be a white, zero-mean Gaussian noise process, with covariance (power spectral density) $\boldsymbol{Q}_{\bar{\boldsymbol{\mathscr{E}}}}(t)$.

The model (13) yields near-linear behavior, since the short-term effects have been averaged out. Therefore, it can be integrated with a large step size (up to one day for LEO satellites). Integration of (13) provides the mean orbital trajectory, i.e., the mean elements $\bar{\boldsymbol{\mathscr{E}}}(t)$ at epoch t. Then, the osculating trajectory is recovered using

$$\boldsymbol{\mathscr{E}}(t) = \bar{\boldsymbol{\mathscr{E}}}(t) + \boldsymbol{\eta}(\boldsymbol{\mathscr{E}}(t), \theta(t)) . \tag{14}$$

2.4. Measurement Model

Next, satellite observations from ground stations are modeled, following [6]. A configuration resorting to a single Ground Station (GS) is considered. These observations are processed in the topocentric frame. The most common ground measurement types, usually implemented by radar, telescope or laser systems, are range s, range-rate $\dot{s}$, azimuth β and elevation δ angles.

Let the topocentric position and velocity vectors of the satellite relative to the GS be, respectively, $\boldsymbol{r}_s = \boldsymbol{T}^s_f(\boldsymbol{r}_f - \boldsymbol{R}_f)$ and $\boldsymbol{v}_s = \boldsymbol{T}^s_f \boldsymbol{v}_f$, where $\boldsymbol{R}_f$ is the station's ECEF position and $\boldsymbol{T}^s_f$ is the rotation matrix from ECEF to East North Zenith (ENZ) topocentric frame.

Let $[s_E, s_N, s_Z]^T$ denote the cartesian components of $\boldsymbol{r}_s$ in topocentric frame. Each unidimensional measurement is given by:

$$\begin{aligned} s &= \sqrt{\boldsymbol{r}_s^T \boldsymbol{r}_s} , \\ \dot{s} &= \frac{\boldsymbol{r}_s^T \boldsymbol{v}_s}{s} , \\ \beta &= \arctan \frac{s_E}{s_N} , \\ \delta &= \arctan \frac{s_Z}{\sqrt{s_E^2 + s_N^2}} . \end{aligned} \tag{15}$$

Finally, by concatenating these observations at time t_k, the measurement model is given by:

$$\boldsymbol{y}(t_k) = \boldsymbol{h}_d(\mathbf{x}(t_k), t_k) + \boldsymbol{v}(t_k) , \tag{16}$$

where $\mathbf{x}$ is the inertial osculating orbital state vector. A transformation of position and velocity vectors from inertial to topocentric frame is, therefore, implicitly employed by $\boldsymbol{h}_d$.

Measurement observations are not ideal, but rather corrupted with measurement noise $\boldsymbol{v}(t_k)$, which quantifies the uncertainty associated with the observations. It is assumed to be a white, zero-mean Gaussian noise process, with covariance $\boldsymbol{R}(t_k)$. For each time instant, the covariance matrix is $\boldsymbol{R} = \operatorname{diag}\left(\sigma_{v_s}^2, \sigma_{v_\beta}^2, \sigma_{v_\delta}^2, \sigma_{v_{\dot{s}}}^2\right)$, where each standard deviation σ_{v_y} is associated to each measurement type y in the set $\{s, \beta, \delta, \dot{s}\}$ (assuming independent unidimensional observations).

It is noted that observations are only available when there exists line of sight between the satellite and the GS. This condition is only verified when the satellite is above the station's local horizon plane.

3. The Unscented Semianalytical Kalman Filter

The idea of coupling SST with filtering algorithms was first proposed in Green's thesis [9], making use of DSST propagator. Green hinted that: 1) this coupling would increase the computational speed of OD procedures; and 2) would also increase the accuracy of filter estimates, because the linearization assumptions used in the algorithms would be better satisfied, given the near-linear behavior of the mean dynamics. Then, Taylor [10] designed and implemented the ESKF, which couples a traditional EKF with DSST. The present work introduces two contributions to the literature: 1) it departs from DSST reliance, and is supported instead by the Semianalytical theory developed by Ely [14, 13] and summarized above; and 2) introduces a novel algorithm coupling an UKF with SST, denominated the Unscented Semianalytical Kalman Filter (USKF).

The fundamental idea of coupling SST with filtering algorithms involves the following time frame definitions [10]:

- **Integration grid :** the time frame used by the semianalytical integrator;
- **Observation grid :** the time frame that contains the arrival times of the observations, to be processed by the filter.

Semianalytical filters operate as follows: 1) the integrator propagates the trajectory along integration grid points at times $t_{k,0}$, originating the nominal trajectory at grid points $\bar{\boldsymbol{\mathscr{E}}}_N(t_{k,0})$; 2) this nominal trajectory is then interpolated, in-between integration grid points, to the arrival times of observations, i.e., interpolated to observation times $t_{k,i}$, for $i = 1, \ldots, M$ (where M is the last point before the next integration time $t_{k+1,0}$), originating the nominal trajectory $\bar{\boldsymbol{\mathscr{E}}}_N(t_{k,i})$ along the observation grid; 3) after the measurements at times $t_{k,i}$ are processed, the filter corrections are propagated through the observation grid, without an explicit update of the nominal trajectory, which is then only updated at the next integration grid point at time $t_{k+1,0}$.

Although Taylor's ESKF makes use of continuous-time state dynamics, the USKF proposed in this work takes discretized dynamics, in view of the traditional implementation of UKFs [16]. Discretization of (13) between integration grid nominal points at times $t_{k,0}$ and $t_{k+1,0}$ yields, resorting to numerical routines for ordinary differential equations,

$$\bar{\boldsymbol{\mathscr{E}}}_N(t_{k+1,0}) = \bar{\boldsymbol{f}}_d(\bar{\boldsymbol{\mathscr{E}}}_N(t_{k,0}), t_{k,0}) + \bar{\boldsymbol{w}}_{k,0} \,. \tag{17}$$

The USKF proposed in this research makes use of the Unscented Transform (UT). Before introducing the filter algorithm, the UT is reviewed. Paraphrasing from [16], the UT is given below, in Algorithm 1. Constants α, β and κ are parameters of the transform. In the present work, these constants are set to $\alpha = 1$, $\beta = 2$ and $\kappa = 0$, cf. [16].

Algorithm 1 Unscented Transform (UT)

Require: Gaussian Random Variable (GRV) $\boldsymbol{x} \in \mathbb{R}^n$ characterized by the distribution $\boldsymbol{x} \sim \mathcal{N}(\bar{\boldsymbol{x}}, \boldsymbol{P_x})$;
Nonlinear function $\boldsymbol{g} : \mathbb{R}^n \mapsto \mathbb{R}^r$;
(α, β, κ).

Ensure: The UT is used for forming the Gaussian approximation

$$\begin{pmatrix} \boldsymbol{x} \\ \boldsymbol{y} \end{pmatrix} \sim \mathcal{N}\left(\begin{pmatrix} \bar{\boldsymbol{x}} \\ \bar{\boldsymbol{y}} \end{pmatrix}, \begin{pmatrix} \boldsymbol{P_x} & \boldsymbol{P_{xy}} \\ \boldsymbol{P_{xy}^T} & \boldsymbol{P_y} \end{pmatrix} \right)$$

of the joint distribution of $\boldsymbol{x}$ and $\boldsymbol{y} \in \mathbb{R}^r$ undergoing the transformation $\boldsymbol{g}(\cdot)$.

1: **function** UT($\boldsymbol{g}$, $\bar{\boldsymbol{x}}$, $\boldsymbol{P_x}$)

2: Form the set of $2n+1$ Sigma Points $\boldsymbol{\mathcal{X}}_i$ as follows:

$$\begin{aligned} \boldsymbol{\mathcal{X}}_0 &= \bar{\boldsymbol{x}} \,, \quad i = 0 \,, \\ \boldsymbol{\mathcal{X}}_i &= \bar{\boldsymbol{x}} + \left[\sqrt{(n+\lambda)\boldsymbol{P_x}}\right]_i \,, \quad i = 1, \ldots, n \,, \\ \boldsymbol{\mathcal{X}}_i &= \bar{\boldsymbol{x}} - \left[\sqrt{(n+\lambda)\boldsymbol{P_x}}\right]_{i-n} \,, \quad i = n+1, \ldots, 2n \,, \end{aligned} \tag{18}$$

where λ is a scaling parameter defined as

$$\lambda = \alpha^2(n+\kappa) - n \,, \tag{19}$$

and $\left[\,\cdot\,\right]_i$ denotes the ith column of the matrix inside the brackets.

3: Compute the associated weights:

$$\begin{aligned} \mathcal{W}_0^{(m)} &= \lambda/(n+\lambda) \,, \\ \mathcal{W}_i^{(m)} &= 1/[2(n+\lambda)] \,, \quad i = 1, \ldots, 2n, \,, \\ \mathcal{W}_0^{(c)} &= \lambda/(n+\lambda) + (1 - \alpha^2 + \beta) \,, \\ \mathcal{W}_i^{(c)} &= 1/[2(n+\lambda)] \,, \quad i = 1, \ldots, 2n \,, \end{aligned} \tag{20}$$

4: Transform each of the Sigma Points with

$$\boldsymbol{\mathcal{Y}}_i = \boldsymbol{g}(\boldsymbol{\mathcal{X}}_i) \,, \quad i = 0, \ldots, 2n \,. \tag{21}$$

5: Finally, compute the statistics:

$$\begin{aligned} \bar{\boldsymbol{y}} &= \sum_{i=0}^{2n} \mathcal{W}_i^{(m)} \boldsymbol{\mathcal{Y}}_i \,, \\ \boldsymbol{P_y} &= \sum_{i=0}^{2n} \mathcal{W}_i^{(c)} (\boldsymbol{\mathcal{Y}}_i - \bar{\boldsymbol{y}})(\boldsymbol{\mathcal{Y}}_i - \bar{\boldsymbol{y}})^T \,, \\ \boldsymbol{P_{xy}} &= \sum_{i=0}^{2n} \mathcal{W}_i^{(c)} (\boldsymbol{\mathcal{X}}_i - \bar{\boldsymbol{x}})(\boldsymbol{\mathcal{Y}}_i - \bar{\boldsymbol{y}})^T \,. \end{aligned} \tag{22}$$

6: **return** $[\bar{\boldsymbol{y}}, \boldsymbol{P_y}, \boldsymbol{P_{xy}}]$

7: **end function**

The operation of the USKF is similar to that of the ESKF. However, the USKF uses Weighted

Statistical Linearization (WSL) [17] to linearize the nominal trajectory and propagate filter corrections, while the ESKF relies on Taylor series linearization. The WSL of (17) around the nominal state $\bar{\boldsymbol{\mathcal{E}}}_N(t_{k,i})$ enables propagation between observation grid time steps,

$$\bar{\boldsymbol{\mathcal{E}}}(t_{k,i+1}) \approx \boldsymbol{A}^N_{k,i}\bar{\boldsymbol{\mathcal{E}}}(t_{k,i}) + \boldsymbol{b}^N_{k,i} + \bar{\boldsymbol{w}}_{k,i}\,, \tag{23}$$

where $\boldsymbol{A}^N_{k,i}$ and $\boldsymbol{b}^N_{k,i}$ are the coefficients of the WSL.

The operations on the integration and observation grids of the proposed USKF are given below. The filter is initialized with an initial state estimate $\bar{\boldsymbol{\mathcal{E}}}(t_0)$ and covariance $\boldsymbol{P}_0$.

3.1. Operations on the Integration Grid

1. At the current time $t_{k,0}$, update the nominal state, $\bar{\boldsymbol{\mathcal{E}}}_{N_{\text{new}}}(t_{k,0})$, for the new integration step, valid on the interval $[t_{k,0}, t_{k+1,0})$, from the old nominal state $\bar{\boldsymbol{\mathcal{E}}}_{N_{\text{old}}}(t_{k,0})$ (defined on the previous integration interval), using

$$\bar{\boldsymbol{\mathcal{E}}}_{N_{\text{new}}}(t_{k,0}) = \bar{\boldsymbol{\mathcal{E}}}_{N_{\text{old}}}(t_{k,0}) + \Delta\bar{\boldsymbol{\mathcal{E}}}^{k-1,M}_{k,0}\,, \tag{24}$$

   where $\Delta\bar{\boldsymbol{\mathcal{E}}}^{k-1,M}_{k,0}$ are the filter corrections from the last observation, at $t_{k-1,M}$, propagated until the current time $t_{k,0}$. Then set the nominal covariance with $\boldsymbol{P}^N_{k,0} = \boldsymbol{P}^-_{k,0}$. The correction $\Delta\bar{\boldsymbol{\mathcal{E}}}^{k-1,M}_{k,0}$ and covariance $\boldsymbol{P}^-_{k,0}$ are found by performing steps 2, 3, 4 and 5 of the observation grid from $t_{k-1,M}$ to $t_{k,0}$;
2. With $\bar{\boldsymbol{\mathcal{E}}}_N(t_{k,0})$ and $\boldsymbol{P}^N_{k,0}$, construct the $2n+1$ nominal sigma points $\boldsymbol{\mathcal{X}}^N_i(t_{k,0})$, cf. (18), and store them in $\boldsymbol{\mathcal{X}}_S$. To simplify the notation, the sigma points are concatenated in vector form as $\boldsymbol{\mathcal{X}}^N(t_{k,0})$. Then, initialize the filter corrections:

$$\begin{aligned}\boldsymbol{\mathcal{X}}_S &= \boldsymbol{\mathcal{X}}^N(t_{k,0})\,,\\ \Delta\bar{\boldsymbol{\mathcal{E}}}^{k,0}_{k,0} &= 0\,;\end{aligned} \tag{25}$$

3. Numerically propagate the nominal trajectory and covariance, using the UT, until time $t = t_{k,0}+\Delta t = t_{k+1,0}$, saving intermediate results at $t = t_{k,\Delta t/3}$ and $t = t_{k,\Delta 2t/3}$, using

$$\left[\bar{\boldsymbol{\mathcal{E}}}_N(t_{k+1}), \boldsymbol{P}^N_{k+1}, \_\right] = \text{UT}\left(\bar{\boldsymbol{f}}_d, \bar{\boldsymbol{\mathcal{E}}}_N(t_k), \boldsymbol{P}^N_k\right)\,, \tag{26}$$

   from initial conditions $\bar{\boldsymbol{\mathcal{E}}}_N(t_{k,0})$ and $\boldsymbol{P}^N_{k,0}$, that were set on step 1. With the state and covariance at the requested times, construct the associated nominal sigma points. With the sets $\boldsymbol{\mathcal{X}}^N(t_{k,0})$, $\boldsymbol{\mathcal{X}}^N(t_{k,\Delta t/3})$, $\boldsymbol{\mathcal{X}}^N(t_{k,2\Delta t/3})$ and $\boldsymbol{\mathcal{X}}^N(t_{k+1,0})$, set up a Lagrange interpolator (with four points) for $\boldsymbol{\mathcal{X}}^N(t)$.

3.2. Operations on the Observation Grid

The operations on the observation grid are triggered by receipt of a new observation. The observation grid procedure is followed in a loop-wise manner until no more observations are available or the next observation is not inside the interval $[t_{k,0}, t_{k+1,0})$, i.e., is later than the next integration time step. In that case, the integration step procedure described above is followed to advance the integration by one grid point. It is noted that, if the first observation comes exactly at time $t = t_{k,0}$, then steps 2 to 5 are ignored for that observation, since the predicted state and covariance are already known from the integration step.

1. Obtain a new observation to process $\boldsymbol{y}(t_{k,i})$;
2. Interpolate $\boldsymbol{\mathcal{X}}^N(t)$ for $t = t_{k,i}$. Get $\boldsymbol{\mathcal{X}}^N(t_{k,i-1})$ from the value stored in $\boldsymbol{\mathcal{X}}_S$. Compute the nominal state and covariance at the two epochs using:

$$\begin{aligned}
\bar{\boldsymbol{\mathcal{E}}}_N(t_{k,i}) &= \sum_{j=0}^{2n}\mathcal{W}^{(m)}_j\boldsymbol{\mathcal{X}}^N_j(t_{k,i})\,,\\
\bar{\boldsymbol{\mathcal{E}}}_N(t_{k,i-1}) &= \sum_{j=0}^{2n}\mathcal{W}^{(m)}_j\boldsymbol{\mathcal{X}}^N_j(t_{k,i-1})\,,\\
\boldsymbol{P}^N_{k,i} &= \sum_{j=0}^{2n}\mathcal{W}^{(c)}_j\Bigg[\Big(\boldsymbol{\mathcal{X}}^N_j(t_{k,i}) - \bar{\boldsymbol{\mathcal{E}}}_N(t_{k,i})\Big)\Big(\boldsymbol{\mathcal{X}}^N_j(t_{k,i}) \\ &\qquad - \bar{\boldsymbol{\mathcal{E}}}_N(t_{k,i})\Big)^T\Bigg]\,,\\
\boldsymbol{P}^N_{k,i-1} &= \sum_{j=0}^{2n}\mathcal{W}^{(c)}_j\Bigg[\Big(\boldsymbol{\mathcal{X}}^N_j(t_{k,i-1}) - \bar{\boldsymbol{\mathcal{E}}}_N(t_{k,i-1})\Big) \\ &\qquad \Big(\boldsymbol{\mathcal{X}}^N_j(t_{k,i-1}) - \bar{\boldsymbol{\mathcal{E}}}_N(t_{k,i-1})\Big)^T\Bigg]\,,\\
\boldsymbol{P}^N_{k,i,i-1} &= \sum_{j=0}^{2n}\mathcal{W}^{(c)}_j\Bigg[\Big(\boldsymbol{\mathcal{X}}^N_j(t_{k,i}) - \bar{\boldsymbol{\mathcal{E}}}_N(t_{k,i})\Big)\Big(\boldsymbol{\mathcal{X}}^N_j(t_{k,i-1}) \\ &\qquad - \bar{\boldsymbol{\mathcal{E}}}_N(t_{k,i-1})\Big)^T\Bigg]\,;
\end{aligned} \tag{27}$$

3. Compute the nominal WSL coefficient $\boldsymbol{A}^N_{k,i}$

$$\boldsymbol{A}^N_{k,i} = \boldsymbol{P}^N_{k,i,i-1}\,\left(\boldsymbol{P}^N_{k,i-1}\right)^{-1}\,; \tag{28}$$

4. Obtain the predicted filter correction and compute the *a priori* mean state $\bar{\boldsymbol{\mathcal{E}}}^-(t_{k,i})$:

$$\begin{aligned}\Delta\bar{\boldsymbol{\mathcal{E}}}^{k,i-1}_{k,i} &= \boldsymbol{A}^N_{k,i}\,\Delta\bar{\boldsymbol{\mathcal{E}}}^{k,i-1}_{k,i-1}\,,\\ \bar{\boldsymbol{\mathcal{E}}}^-(t_{k,i}) &= \bar{\boldsymbol{\mathcal{E}}}_N(t_{k,i}) + \Delta\bar{\boldsymbol{\mathcal{E}}}^{k,i-1}_{k,i}\,;\end{aligned} \tag{29}$$

5. Discretize the process noise covariance and compute the predicted covariance:

$$\begin{aligned}\boldsymbol{Q}_d(t_{k,i}, t_{k,i-1}) &= \boldsymbol{A}^N_{k,i}\,\boldsymbol{Q}(t_{k,i})\,\left(\boldsymbol{A}^N_{k,i}\right)^T\cdot(t_{k,i} - t_{k,i-1})\,,\\ \boldsymbol{P}^-_{k,i} &= \boldsymbol{A}^N_{k,i}\,\boldsymbol{P}^+_{k,i-1}\,\left(\boldsymbol{A}^N_{k,i}\right)^T + \boldsymbol{Q}_d(t_{k,i}, t_{k,i-1})\,,\end{aligned} \tag{30}$$

   where $\boldsymbol{Q}(t_{k,i})$ is the continuous-time noise covariance matrix;
6. Consider the measurement function with respect to the mean equinoctial state as

$$\bar{\boldsymbol{h}}(\bar{\boldsymbol{\mathcal{E}}}(t)) = \boldsymbol{h}_d\Big(\boldsymbol{X}\big(\bar{\boldsymbol{\mathcal{E}}}(t) + \boldsymbol{\eta}(\bar{\boldsymbol{\mathcal{E}}}(t), \theta(t))\big), t\Big)\,, \tag{31}$$

where $\boldsymbol{X}$ is the conversion from osculating $\boldsymbol{\mathscr{E}}$ to $\mathbf{x}$. Do the traditional UKF update step:

$$
\begin{aligned}
&[\hat{\boldsymbol{y}}(t_{k,i}), \boldsymbol{P_y}, \boldsymbol{P_{\mathscr{E}y}}] = \mathrm{UT}\left(\bar{\boldsymbol{h}}, \bar{\boldsymbol{\mathscr{E}}}^{-}(t_{k,i}), \boldsymbol{P}_{k,i}^{-}\right) , \\
&\boldsymbol{K} = \boldsymbol{P_{\mathscr{E}y}} \left[\boldsymbol{P_y} + \boldsymbol{R}_{k,i}\right]^{-1} , \\
&\Delta\bar{\boldsymbol{\mathscr{E}}}_{k,i}^{k,i} = \Delta\bar{\boldsymbol{\mathscr{E}}}_{k,i}^{k,i-1} + \boldsymbol{K}\left(\boldsymbol{y}(t_{k,i}) - \hat{\boldsymbol{y}}(t_{k,i})\right) , \\
&\bar{\boldsymbol{\mathscr{E}}}^{+}(t_{k,i}) = \bar{\boldsymbol{\mathscr{E}}}^{-}(t_{k,i}) + \Delta\bar{\boldsymbol{\mathscr{E}}}_{k,i}^{k,i} , \\
&\boldsymbol{P}_{k,i}^{+} = \boldsymbol{P}_{k,i}^{-} - \boldsymbol{K}\boldsymbol{P_y}\boldsymbol{K}^{T} .
\end{aligned}
$$

where $\boldsymbol{R}_{k,i}$ is the measurement noise covariance;

7. Save the sigma points of the current step into $\boldsymbol{\mathcal{X}}_S$, i.e. $\boldsymbol{\mathcal{X}}_S = \boldsymbol{\mathcal{X}}^N(t_{k,i})$, to be used in the next observation.

The algorithm provides, after each update step, the estimated equinoctial mean state and covariance $\bar{\boldsymbol{\mathscr{E}}}^{+}(t_{i,k})$ and $\boldsymbol{P}_{k,i}^{+}$. It is possible to transform these quantities to the osculating state-vector form, using [10]:

$$
\begin{aligned}
\mathbf{x}^{+}(t_{k,i}) &= \boldsymbol{X}\Big(\bar{\boldsymbol{\mathscr{E}}}^{+}(t_{k,i}) + \boldsymbol{\eta}\big(\bar{\boldsymbol{\mathscr{E}}}^{+}(t_{k,i}), \theta(t_{k,i})\big)\Big) , \\
\boldsymbol{P}_{\mathbf{x}}^{+}(t_{k,i}) &= \boldsymbol{G}\left(\bar{\boldsymbol{\mathscr{E}}}^{+}(t_{k,i})\right) \boldsymbol{P}_{k,i}^{+} \boldsymbol{G}^{T}\left(\bar{\boldsymbol{\mathscr{E}}}^{+}(t_{k,i})\right) ,
\end{aligned} \tag{32}
$$

where $\boldsymbol{G} = (\partial\mathbf{x}/\partial\boldsymbol{\mathscr{E}})\left(\partial\boldsymbol{\mathscr{E}}/\partial\bar{\boldsymbol{\mathscr{E}}}\right)$. Partials $\partial\boldsymbol{\mathscr{E}}/\partial\bar{\boldsymbol{\mathscr{E}}}$ are obtained by finite differencing.

4. Simulation Results

In this section, the most significant simulation tests and results obtained throughout this work are shown and discussed.

4.1. Simulation Environment

In the simulation environment, filters run at a fixed step of 5 seconds. In the absence of station availability, only the filter predict step is employed. Once line of sight is restored, the filters resume their predict-update cycle normally.

In order to conduct the simulation studies, a reference (true) orbital trajectory needs to be defined. This reference trajectory is used to generate noisy observations, which are obtained by adding random noise to the ideal measurements computed with the true trajectory according to (16). The standard deviations of measurement errors are 100 m, 0.02° and $10\,\mathrm{cm\,s^{-1}}$, for range, azimuth/elevation and range-rate, respectively. These noise statistics represent typical values of LEO tracking radar systems [5]. Furthermore, the reference trajectory is also used for evaluating filter performance, through the Root Mean Square Error (RMSE) metric. The RMSE at time t_k is given by

$$
\mathrm{RMSE}(t_k) = \sqrt{\frac{1}{N}\sum_{i=i}^{N} \|\boldsymbol{x}(t_k) - \hat{\boldsymbol{x}}(t_k)\|^2} , \tag{33}
$$

where $\boldsymbol{x}(t_k)$ is the true state (velocity/position vector or equinoctial element), $\hat{\boldsymbol{x}}(t_k)$ is the filter estimate and N is the number of independent Monte Carlo (MC) simulation runs. Averaging the RMSE along the full simulation time span yields $\overline{\mathrm{RMSE}}$.

The single ground station is located in Lisbon. The site's geodetic coordinates are: altitude $h = 0\,\mathrm{m}$, latitude $\phi_{gd} = 38.7°$ and longitude $\lambda = -9.2°$.

A realistic reference trajectory is obtained using the Cowell propagator provided by the General Mission Analysis Tool (GMAT) software, considering a complete force model, which comprises a 180×180 gravitational field, atmospheric drag with Jacchia Roberts density model, Solar Radiation Pressure (SRP) with cannonball (spherical) model, third-body perturbations from the Sun, Moon and Jupiter, solid and pole Earth tides and relativistic corrections. A Sun-synchronous LEO is considered. The osculating initial conditions are provided in Table 1.

Initial orbital conditions	
Epoch	6 April, 2000 11:00:00 UTC
Osculating Keplerian set $(a, e, i, \Omega, \varpi, \nu)$	(7178 km, 0.03, 98.6°, 20°, 0°, 0°)

Table 1: Initial epoch and orbital state.

The physical properties of the satellite (held constant throughout the simulations) are shown in Table 2.

Satellite Properties	Numerical Value
Mass m	25 kg
Drag Area A_{drag}	$0.5\,\mathrm{m}^2$
Coefficient of Drag C_D	2.0
SRP Area A_{SRP}	$0.5\,\mathrm{m}^2$
SRP Coefficient of Reflectivity C_R	1.5

Table 2: Physical properties of the satellite. It is noted that A_{SRP} and C_R are only defined to be used in the GMAT reference trajectory procedure, since SRP is not part of the filter dynamics.

4.2. Cowell and Semianalytical Propagation Results

Before evaluating the performance of Semianalytical filters, the accuracy and computational cost of the implemented Semianalytical propagator are benchmarked against a Cowell propagator, which was also implemented in this study.

The Cowell osculating trajectory is obtained by integrating the model (2), whereas the Semianalytical osculating trajectory is obtained by integrating model (13) and then using (14).

Both propagators use the Runge-Kutta 5(4) integration solver, with relative and absolute tolerances set to 10^{-3} and 10^{-6}, respectively. Both propagators are set up with the same force model, comprising a 5×5 gravitational field and atmospheric drag.

The developed Semianalytical propagator is also compared with DSST, which is an established semi-analytical propagator icluded in the Orbit Extrapolation Kit (Orekit) Java flight dynamics library. DSST is tuned with an equivalent force model.

Following the tuning procedure described by Ely in [14], the Semianalytical DFT lengths $N_{Z,D}$, N_T and M_T, and the order of the numerical quadrature N_{quad} are found by trial and error. The following values were found to yield good results: $N_{Z,D} = 16$, $N_T = 16$, $M_T = 16$ and $N_{\text{quad}} = 20$. It is noted that using greater values would provide marginal gains, at best, while being more computationally expensive.

4.2.1 Propagation Accuracy

First, the Semianalytical mean element propagation is compared with the equivalent propagation provided by DSST. The averaged $\overline{\text{RMSE}}$ for each mean equinoctial element, relative to the DSST baseline, is shown in Table 3 for a 7500-day propagation. It is seen that both propagators yield very similar results, which validates the mean element propagation of the present Semianalytical model.

Equinoctial mean element	$\overline{\text{RMSE}}$
$\bar{a}$	5.152×10^{-10}km
$\bar{h}$	2.033×10^{-6}
$\bar{k}$	2.087×10^{-6}
$\bar{p}$	4.665×10^{-5}
$\bar{q}$	4.562×10^{-5}
$\bar{\lambda}$	3.235×10^{-6}rad

Table 3: $\overline{\text{RMSE}}$ of mean element propagation of the developed Semianalytical propagator, relative to DSST, for a 7500-day simulation period.

Next, the osculating trajectories outputted by the developed Semianalytical propagator and DSST are compared to the Cowell trajectory. The time evolution of the osculating position and velocity RMSE are depicted in Figure 1 for a 1-day propagation, taking the Cowell trajectory as reference. For comparison, the figure also shows an analytical mean-to-osculating map based on Brouwer analytical theory (formulated in Appendix G of [18]), coupled with the mean element propagation, provided by the developed Semianalytical propagator. This analytical map comprises a 2 × 0 (J2) gravitational field.

This simulation evidences that DSST captures the short-term effects better than the developed Semianalytical propagator. This may be explained by the fact that the DSST mean-to-osculating map is more complete, containing second-order terms of some perturbations [12], whereas the developed propagator was truncated to first order. Nevertheless, they both outperform the analytical mean-to-osculating map.

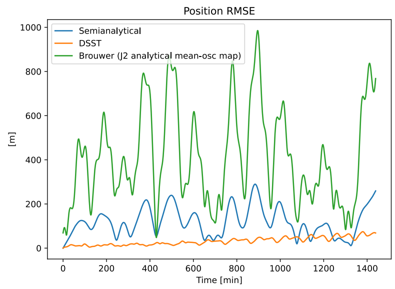

Figure 1: Osculating position RMSE of different propagation theories, compared relative to Cowell propagation. Orange and blue lines represent, respectively, the error provided by DSST and the developed Semianalytical propagators. The green line illustrates an analytical mean-to-osculating map based on Brouwer analytical theory [18], coupled with mean element propagation of the developed Semianalytical propagator. 1-day simulation.

4.2.2 Computational Cost

The propagation analysis is concluded with a CPU computation time comparison. Figure 2 illustrates the CPU computation time for different propagation periods (from a 1-day to a 7-day propagation), for both Cowell and Semianalytical propagators. The trajectory is outputted at a requested fixed step of 60 seconds. The efficiency of the Semianalytical scheme is clearly evidenced.

To conclude, an efficient Semianalytical implementation was achieved. Nonetheless, this efficiency comes with a slight loss in accuracy, when compared to Cowell propagation with a similar force model. Depending on the mission requirements, the propagator that offers the best trade-off between accuracy and computational effort is to be favored.

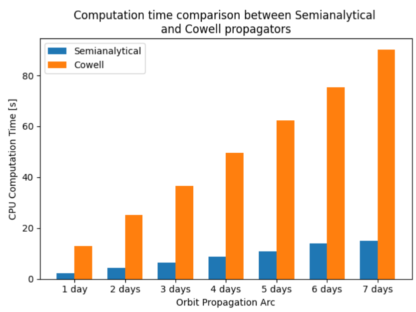

Figure 2: CPU computation time comparison between the developed Cowell and Semianalytical propagators for propagation arcs from 1 day to 7 days. The orbital outputs are requested every 60 seconds. The simulation was programmed in a Python environment and conducted on a laptop computer with 8GB RAM and Intel® i7-4210U, 1.7 GHz processor.

4.3. Cowell and Semianalytical Filter Results

The USKF designed in Section 3 is compared with Taylor's ESKF (adapted to the present Semianalytical propagation scheme), as well as Cowell Extended and Unscented Kalman Filters (denoted by EKF and UKF, respectively).

The filter initialization procedure is chosen to be self starting, in the sense that the filters should be able to initialize taking into account only the ground station available observational data. The procedure comprises Gauss's Initial Orbit Determination (IOD) method [5], followed by a batch Least-Squares Differential Correction method [5]. A batch of 15 observations (75 seconds) is considered.

The measurement noise covariance matrix $\boldsymbol{R}$, to be used in the update steps, is readily constructed referring to the same standard deviations considered for measurement noise generation.

Determination of the process noise covariance matrix $\boldsymbol{Q}$ is relatively more complex. A more trial and error approach was adopted to define its diagonal entries, adjusting the values manually with the help of simulations. The following osculating covariance, in state-vector form, was found

$$\boldsymbol{Q}_{\mathbf{x}} = \begin{bmatrix} 10^{-9}\boldsymbol{I}_{3\times3} & \mathbf{0}_{3\times3} \\ \mathbf{0}_{3\times3} & 10^{-12}\boldsymbol{I}_{3\times3} \end{bmatrix}, \tag{34}$$

where the velocity and acceleration entries are given, respectively, in $\mathrm{km\,s^{-1}}$ and $\mathrm{km\,s^{-2}}$.

This covariance is then transformed to the mean equinoctial space space, for use with Semianalytical filters, using $\boldsymbol{Q}_{\bar{\boldsymbol{\mathcal{E}}}} = \boldsymbol{G}^{-1}\boldsymbol{P}_{\mathbf{x}}(\boldsymbol{G}^{T})^{-1}$, where $\boldsymbol{G} = (\partial\mathbf{x}/\partial\boldsymbol{\mathcal{E}})\left(\partial\boldsymbol{\mathcal{E}}/\partial\bar{\boldsymbol{\mathcal{E}}}\right)$. This transformation ensures equivalent process noise between the osculating and mean dynamics, which allows for a fair comparison of filter results.

Figure 3 presents the time evolution of the osculating position RMSE for a 7-day filtering simulation (only one MC run was made). Table 4 further provides the trajectory averaged position $\overline{\mathrm{RMSE}}$ for the same simulation run, as well as the error in each component of the satellite-based RSW frame (R - Radial, S - Along-Track and W - Cross-Track).

	Position RMSE [m]			
Filter	R	S	W	3D
EKF	59.32	878.28	35.02	880.97
UKF	59.51	871.41	35.32	874.15
ESKF	94.91	582.10	89.81	596.59
USKF	92.44	537.54	88.86	552.62

Table 4: Trajectory averaged position $\overline{\mathrm{RMSE}}$ for the same simulation run illustrated in Figure 3. The error in each component of the RSW frame is also provided.

In this simulation, Semianalytical filters outperformed Cowell filters, with an accuracy gain of around 300 m. Moreover, both for Cowell and Semianalytical filters, the unscented algorithms slightly outperformed the extended ones. The superiority of Semianalytical filters may be explained by the fact that the mean dynamics, estimated in the ESKF and USKF, are more linear than the osculating dynamics, estimated in Cowell filters. Therefore, they better satisfy the linearization procedures of filtering predict steps [9].

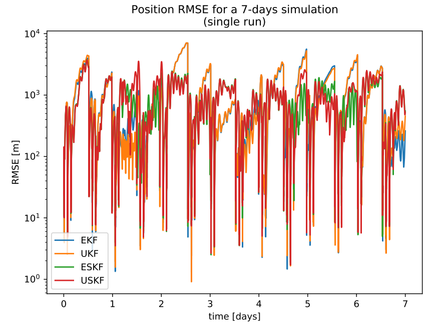

Figure 3: Time evolution of the position RMSE of the filtered trajectories outputted by EKF (blue), UKF (yellow), ESKF (green) and USKF (red) relative to the reference trajectory, for a single MC run. The simulation length is 7 days.

Figure 4 plots the time evolution of the position RMSE when the considered estimate is simply obtained by inversion of the measurement function (using only range, azimuth and elevation observations), for a single ground station pass. Clearly, the error of these rough and unfiltered estimates is substantially worse than the error obtained with filters, which further evidences the performance and relevance of the implemented algorithms.

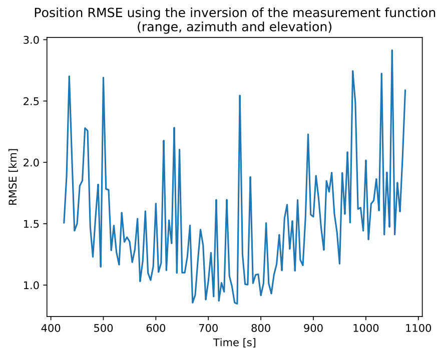

Figure 4: Position RMSE considering orbital estimates obtained directly by inversion of the measurement function (with range, azimuth and elevation), for a single ground station pass. 100 MC simulations runs were performed.

4.4. Summary of Other Results

The main results of the present study were presented and discussed above. Below is a summary of additional results, drawn from complementary studies (not shown).

The sensitivity of the filters to initialization errors was studied. This is relevant, since, in the context of sub-optimal Kalman filters, bad estimates may lead to filter divergence. It was found that Cowell filters are able to converge in much worse initialization environments than Semianalytical filters. For instance, Cowell filters converged with initial position errors of up to 10 000 km, whereas both Semianalytical filters diverged when position errors of 1000 km were provided. The existence of long periods of station unavailability may explain this drawback, since the estimation of mean trajectories in Semianalytical filters is slightly slower to converge than Cowell estimation of osculating trajectories, due to the inherent averaging procedure associated to the mean dynamics. It is noted that, for the conditions of Table 1, GS passes last, approximately, between 10 to 15 minutes, and one orbital period is $\sim$ 100 minutes.

Further tests comparing the performance of ESKF and USKF revealed that the latter converges faster to the true trajectory and tends to be less prone to destabilization than the ESKF, indicating that it is more stable and robust.

5. Conclusions

The present research studied the development of OD solutions able to localize LEO satellites, in the absence of GNSS sensors, resorting to ground station data, through the use of Cowell and Semianalytical orbital propagation schemes, coupled with sub-optimal Kalman filters, namely, the EKF and UKF.

The SST used in this work was proposed by Todd Ely, and diverges from more traditional SSTs in the sense that: 1) the averaging of the mean element rates is achieved through numerical quadrature; and 2) the short-periodic functions are computed numerically with FFT algorithms. Compared to DSST, Ely's theory is not as efficient, since numerical quadrature and FFT evaluations require sampling of the orbital state function. Furthermore, simulations performed in this research indicated that DSST's mean-to-osculating map is more complete and better captures short-term periodic effects. The extension of Ely's theory to second order may improve its propagation accuracy, and is left as future work.

Under the designed simulation environment, it was found that, when initialized with a fairly good estimate, Semianalytical filters outperformed Cowell filters, in terms of accuracy. This suggests that, when using reduced force models, Semianalytical filters are better able to estimate the long-term evolution of the dynamical state. Moreover, it was also shown that Semianalytical propagation schemes are much more efficient, in view of the larger allowable integration step sizes.

Compared to the ESKF, the proposed USKF shows more robustness to destabilization and to initialization errors. It also converges faster to the true state.

Ultimately, the fundamental conclusion to be drawn from this study is that substantial improvements in efficiency can be attained, without loss of accuracy, by the application of SST within Orbit Determination problems.

References

[1] Jerome Vetter. Fifty years of orbit determination: Development of modern astrodynamics methods. *J. Hopkins Appl. Tech. D*, 27, January 2007.

[2] Oliver Montenbruck. Space applications. In *Springer Handbook of Global Navigation Satellite Systems*, pages 933–964. Springer International Publishing, May 2017.

[3] Weichao Zhong and Pini Gurfil. Mean orbital elements estimation for autonomous satellite guidance and orbit control. *Journal of Guidance Control Dynamics*, 36:1624–1641, November 2013.

[4] Srinivas J Setty, Paul J Cefola, Oliver Montenbruck, and Hauke Fiedler. Application of semi-analytical satellite theory orbit propagator to orbit determination for space object catalog maintenance. *Advances in Space Research*, 57(10):2218–2233, 2016.

[5] D.A. Vallado and W.D. McClain. *Fundamentals of Astrodynamics and Applications.* Space Technology Library. Microcosm Press & Springer, 4^{th} edition, 2013.

[6] Oliver Montenbruck and Eberhard Gill. *Satellite Orbits*, volume 1. Springer-Verlag GmbH, January 2000.

[7] Huimin Chen, Genshe Chen, Erik Blasch, and Khanh Pham. Comparison of several space target tracking filters. In *Sensors and Systems for Space Applications III*, volume 7330. International Society for Optics and Photonics, 2009.

[8] Sofya Spiridonova, Michael Kirschner, and Urs Hugentobler. Precise mean orbital elements determination for LEO monitoring and maintenance. 2014.

[9] Andrew Joseph Green. *Orbit determination and prediction processes for low altitude satellites.* PhD thesis, Massachusetts Institute of Technology, 1979.

[10] Steve Taylor. Semianalytical satellite theory and sequential estimation. Master's thesis, Massachusetts Institute of Technology, September 1981.

[11] Zachary James Folcik. Orbit determination using modern filters/smoothers and continuous thrust modeling. Master's thesis, Massachusetts Institute of Technology, 2008.

[12] D. Danielson, C. Sagovac, Beny Neta, and L. Early. Semianalytic satellite theory (SST): Mathematical algorithms. *Naval Postgraduate School*, January 1995.

[13] Todd A Ely. Mean element propagations using numerical averaging. *The Journal of the Astronautical Sciences*, 61(3):275–304, 2014.

[14] Todd A Ely. Transforming mean and osculating elements using numerical methods. *The Journal of the Astronautical Sciences*, 62(1):21–43, 2015.

[15] Ali H Nayfeh. *Perturbation methods.* John Wiley & Sons, 2008.

[16] Eric A Wan, Rudolph Van Der Merwe, and Simon Haykin. The unscented Kalman filter. *Kalman filtering and neural networks*, 5(2007):221–280, 2001.

[17] Rudolph Van Der Merwe. *Sigma-point Kalman filters for probabilistic inference in dynamic state-space models.* PhD thesis, OGI School of Science & Engineering at OHSU, 2004.

[18] H. Schaub and J. L. Junkins. *Analytical Mechanics of Space Systems*, volume 1. AIAA, 1^{st} edition, 2003.